ADVANCED FUNCTIONAL MATERIALS
www.afm-journal.de

Chameleon-Inspired, Dipole Moment-Increasing, Fire-Retardant Strategies Toward Promoting the Practical Application of Radiative Cooling Materials

Wei Cai, Liangyuan Qi, Tianyang Cui, Bicheng Lin, Mohammad Ziaur Rahman, Xin Hu, Yang Ming, Ah Pun Chan, Weiyi Xing, De-Yi Wang,* Bin Fei,* and Jintu Fan*

Toward addressing the aesthetic demand, IR emissivity, and fire hazards of radiative cooling materials in the practical application, chameleon-inspired is tactfully employed, dipole moment-increasing, and fire-retardant strategies to manufacture an advanced polyurea-based composite coating through incorporating thermochromic microcapsules, boron nitride nanosheets, and montmorillonite nanosheets. The chameleon-inspired thermochromic microcapsules and admirable IR emissivity (supported by the original IR emittance spectra) realized by the increasing dipole moment allow the composite coatings to spontaneously adjust the solar absorption and reflection during hot daytime, while enabling high-efficiency radiative cooling throughout the day. The IR emissivity higher than most literature is attributed to the strong interfacial interactions within polyurea composite coatings which improve the dipole moment of C—O—C, Si—O, and B—N bonds by increasing the distance between the centers of positive and negative charges, thus producing more IR emissions. Furthermore, the thermally melted montmorillonite nanosheets can form a ceramic protective layer enhanced by boron nitride nanosheets, further suppressing combustion behavior to improve the fire safety performance of polyurea coatings. The integration of thermochromic functionality, high fire safety, and admirable IR emissivity not only contribute to promoting the practical application of radiative cooling materials, but also provide a precious reference route to design high IR emissivity.

1. Introduction

After solving the basic survival problem such as food and clothing, people begin to seek more and more comfortable living conditions, along with rapid economic development globally. In hot summer, a comfortable building temperature will significantly improve people's happiness, avoiding the fearful illness caused by high-temperature weather. It is interesting that, in China, young people have claimed "Air conditioning system save their lives in summer", which strongly expresses a demand for the cool building temperature. However, air cooling systems consume 15% of electricity generated globally and account for 10% of global greenhouse gas emissions.[1] Meanwhile, a good deal of CO_2 gas released by the air cooling systems will uninterruptedly exacerbate the fearful greenhouse effect, bringing higher temperatures. As presented by the form of a vicious circle, the higher temperature caused by the greenhouse effect needs more use of air conditioning systems. Beyond all doubt, realizing a comfortable building temperature with

W. Cai, M. Z. Rahman, X. Hu, Y. Ming, B. Fei, J. Fan
School of Fashion and Textiles
The Hong Kong Polytechnic University
Kowloon, Hong Kong SAR 999077, P. R. China
E-mail: bin.fei@polyu.edu.hk

L. Qi, T. Cui, B. Lin, W. Xing
State Key Laboratory of Fire Science
University of Science and Technology of China
Hefei 230026, P. R. China
E-mail: xingwy@ustc.edu.cn

A. P. Chan
Faculty of Design and Environment
Technological and Higher Education Institute of Hong Kong
Hong Kong SAR, P. R. China

D.-Y. Wang
IMDEA Materials Institute
C/Eric Kandel, 2, Getafe, Madrid 28906, Spain
E-mail: deyi.wang@imdea.org

The ORCID identification number(s) for the author(s) of this article can be found under https://doi.org/10.1002/adfm.202412902

DOI: 10.1002/adfm.202412902

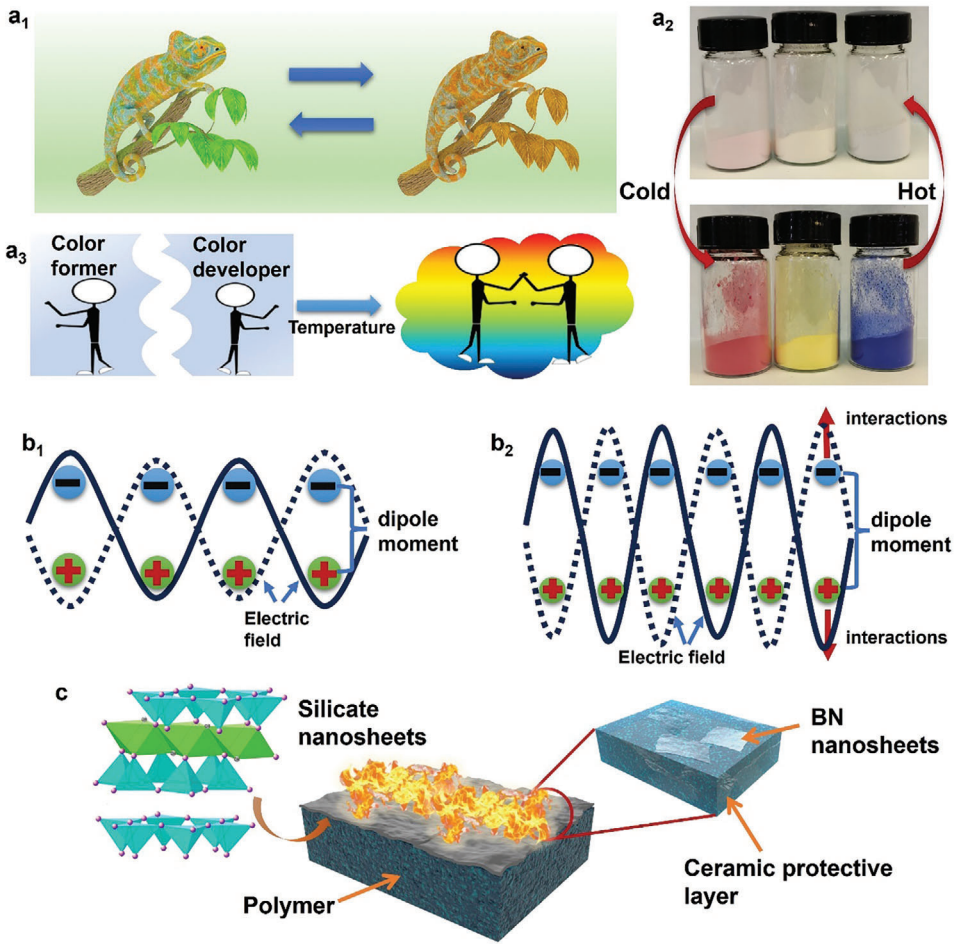

Figure 1. Schematic for chameleon-inspired, dipole moment-increasing, fire-retardant strategies. a_1) The appearance change of the chameleon corresponding to the environment; a_2) The color change process of TC microcapsules, presenting bright and light colors at different temperatures; a_3) The schematic for the combination and separation of color former and color developer, attributed to the switch between solid and melting phase of fatty alcohol; b_1,b_2) The schematic of dipole moment, demonstrating that the interactions promote the inhomogeneous distribution of electric charge; c) The schematic for the synergistic effect of MMT and BN nanosheets in flame retardancy performance, indicating that MMT nanosheets will thermally melt into a ceramic protective layer enhanced by BN nanosheets with extremely high thermal stability.

an energy-free approach has become the key solution to resolve the above dilemma.

Recently, the radiative cooling technology that can radiate an object's heat to outer space used as the cold source has been regarded as the effective solution to energy-free decrease the building temperature.[2,3] There are two operating modes, i.e., daytime and nighttime. The difficulty of daytime radiative cooling technology is significantly larger than the nighttime modes, attributed to the high demand for reflectivity. For achieving high solar reflectivity, a porous structure is usually employed as the main approach. For example, Wang and Hu et al. report the solar reflectivity of up to 99.6% and >96.0% in porous aluminum oxide (Al_2O_3) coatings.[3,4] Besides, by adding white fillers, the solar reflectivity of up to 93% is also achieved in acrylic coating.[5] However, the high reflectivity in solar waveband causes a white appearance that is not conducive to aesthetic needs. The dilemma between high reflectivity and aesthetic appearance has brought a huge challenge for the practical application of radiative cooling materials. In nature, chameleon is capable of changing its color to conform the different environments (**Figure 1**-a1), attributed to the change of pigment cells.[6] When the chameleon senses changes in the surrounding environment, such as light, temperature, humidity, and external stimuli, its nervous system sends signals that cause various pigment cells in the skin to change, thereby changing color. Obviously, once the color-changing function is introduced to radiative cooling materials, the contradiction between high reflectivity in UV–vis waveband and aesthetic demand can be effectively addressed. Recently, thermochromic (TC) microcapsules based on the phase change characteristic of fatty alcohol have presented a huge potential to adjust the reflectivity and color according to the environment temperature (Figure 1-a2).[7] At different temperatures, fatty alcohol will be in a molten state or solidification state. The color former agents (such as fluorane and spiro lactone) are not dissolved into fatty alcohol in any state, while color developer agents (such as bisphenol A and salicylic acid) can be dissolved into molten fatty alcohol. In other words, in the solid state of fatty alcohol, color former agents will react with color

developer agents to present a colored appearance. However, in the molten state of fatty alcohol, color former agents aren't able to touch color developer agents, thus showing their own color. Therefore, based on the different environment temperatures, the combination and separation regulation of color formers and color developers successfully make thermochromic microcapsules selectively absorb and reflect solar energy, similar to the regulation mechanism of pigment cell in chameleon (Figure 1-a3). There are many research works that introduce thermochromic microcapsules to polymer resin, thus preparing thermally-managed composite materials that can be used as building coatings.[8,9] For example, Wang et al. added the thermochromic microcapsules in poly(vinylidene fluoride-co-hexafluoropropylene) to prepare porous film and electrospun fabric, balancing the aesthetic demand and radiative cooling performance.[7,10] Even with the progress of polymer/thermochromic microcapsules composite coatings, there are still three key challenges to promote its practical application. First, the thermochromic microcapsules (TCM) only adjust the solar absorption and reflection, and a high IR emissivity is still required for composite coatings.[9] Second, the preparation of polymer/TCM composite coatings needs an eco-friendly and constructible method to avoid environment pollution, applicable to existing building surfaces. Third, related tightly to buildings, the fire safety of radiative cooling materials is extremely important. Recently, national governments and institutions have set strict laws and standards for the flame retardancy performance of building materials, such as ASTM E84, ASTM E119-22, and ASTM E1537. Therefore, the high flammability in polymer/TCM composite coatings which are composed of organic elements must be resolved.

Due to the high resistance to water, well anti-explosion performance, and solvent-free craft, polyurea coating has been applied in the fields related to people's lives and national defense. The molecule chain of polyurea (PUA) coating can be divided into soft and hard segments, composed of fatty polyether and carbamido bonds, respectively. The IR characteristic peaks of fatty polyether are located at 1150–1060 cm^{-1} (stretching vibration of C—O—C bond) and 1000–650 cm^{-1} (out-of-plane bending vibration of C-H bond), overlapping accurately with the transparency atmospheric window. It is reported widely that the IR intensity of the characteristic peak is determined by the changing size of the dipole moment, which is corresponding to the energy levels generated by molecular vibrations (Figure 1-b1).[11] Fortunately, the N-H structure in the carbamido group (i.e., hard segment) of PUA resin can form hydrogen-bond interactions with O atoms of C—O—C bonds to promote the inhomogeneous distribution of electric charge, which not only disrupts vibrational symmetry and increases vibrational asymmetry but also increases the distance between positive and negative charges, ultimately enhancing the change of the dipole moment during molecular vibrations to bring more IR emission (Figure 1-b2).[11,12] Therefore, using PUA resin to design the radiative cooling coating can potentially achieve a high IR emissivity. In addition, attributed to the appropriate viscosity and curing rate, PUA coating with the strong adhesion provided by the carbamido bonds is easily applied to the surface of diversified materials and buildings. In other words, it is viable to employ PUA-based radiative cooling materials further modifying the surface of existing buildings, addressing the workability problem.

At present, some research works have reported that incorporating boron nitride (BN) nanosheets into polymer resin not only increases the solar reflectivity but also enhances the IR emissivity, attributed to its large bandgap and characteristic IR absorption of B—N bond.[5] For example, by introducing BN nanosheets, Felicelli et al. synthesized a ultra-white acrylic paint that achieves solar reflectivity of 97.9% and IR emissivity of 83.0% with only 150 μm thickness.[5] In addition, establishing a porous structure in polydimethylsiloxane also realizes the win-win situation of high reflectivity (93%) and IR emissivity (96%).[13] The highlighted IR emissivity is due to the characteristic absorption of B—N and Si—O bonds. However, these research works have neglected the flame retardancy of B—N and Si—O bonds. First, polydimethylsiloxane or silicate can be thermally melted into a ceramic protective layer to effectively isolate the heat, fire, and pyrolysis products.[14] Second, with the layered nanomaterial and large specific surface area, BN nanosheets with extremely high thermal stability can enhance the mechanical strength of polymer or silicate fusants (Figure 1c).[15] Apart from the above-mentioned things, the exposed amino groups in BN nanosheets and hydroxyl groups in silicate nanosheets will form strong strong interfacial interactions with polymer molecules to promote the inhomogeneous distribution of electric charge in chemical bonds, thus enhancing the change of dipole moment (Figure 1-b2).

Therefore, in this work, we first introduce Si—O and B-O bonds onto the surface of commercial TC microcapsules to decrease the fire hazards of TC microcapsules, by synthesizing a Si/B-containing shell. Then, we further combine BN and montmorillonite (MMT) nanosheets with PUA resin to prepare thermochromic and flame-retardant PUA-based composite coatings, by a solvent-free approach. Obviously, due to the thermochromic function, the designed composite coatings can spontaneously adjust the solar absorption and reflection, according to environment temperature. Meanwhile, the synergistic effect of BN and MMT nanosheets is capable of suppressing the fire hazards of PUA composite coatings. Most importantly, it is expected that the hydroxyl group of MMT nanosheets and the amino group of BN nanosheets, as well as the carbamido group of PUA molecule will affect the C—O—C bonds to increase the dipole moment, further producing more IR emission. Beyond all doubt, the integration of chameleon-inspired, dipole moment-increasing, and fire-retardant strategies significantly promotes the practical application of radiative cooling technology, by meeting the aesthetic demand, admirable IR emissivity, and high fire safety.

2. Results and Discussion

2.1. Characteristics of Fillers and PUA Composite Coatings

As presented in Figure S1 (Supporting Information), pure TC microcapsules are first dispersed in a water solution by combining mechanical stir and sonication. Then, tetraethyl orthosilicate (TEOS) and aminopropyltriethoxysilane (APTES) are added to the above TC microcapsule suspension. APTES can react with H_2O to produce OH^- ion, thus promoting the reaction between TEOS and APTES. Reacting at room temperature for 6 h, boric acid is introduced to chelate with the amino group of APTES, synthesizing SiB-TC

microcapsules. In addition, SiB-TC microcapsules are also immersed in the ethyl alcohol solution with pH = 1 to destroy the thermochromic function, further preparing the control samples. The surface morphology of pure TC microcapsules with a blue appearance is observed by scanning electron microscope (SEM), demonstrating the smooth feature (**Figure** 2-a1). The grain size of pure TC microcapsules is uneven, from 1 to 10 µm. Meanwhile, the obvious sunken structure is also presented, due to the phase change of fatty alcohol.[16] Modified by TEOS, APTES, and boric acid, the surface morphology of SiB-TC microcapsules changes to rough from smooth (Figure 2-a2). Further, the particle scale is not changed. As presented by SEM spectra, the surface elements of SiB-TC microcapsules contain C, O, N, Si, and B (Figure 2b; Figure S2, Supporting Information). The C, N, and O elements are from the TC microcapsules themselves, while Si and B elements are introduced by the modification of TEOS, APTES, and boric acid. It is found that the distribution of Si element perfectly matches the morphology of SiB-TC microcapsules. Detected by the Energy Dispersive Spectrometer (EDS) spectrum, the mass ratios of B and Si elements are 1.61 and 2.09 wt.% (Figure S3, Supporting Information). Of course, due to the substrate materials, the mass ratio of B and Si elements is not accurate. However, these results still strongly confirm that the TC microcapsules are modified successfully by APTES and boric acid. The Fourier transform infrared spectroscopy (FTIR) spectra of pure TC and SiB-TC microcapsules are also compared (Figure S4, Supporting Information). The introduction of a Si/B-containing shell significantly enhances the characteristic peaks located in 2918 cm^{-1} and 2850 cm^{-1}, attributed to the existence of the CH_2- group. The characteristic peak near 1071 cm^{-1}in SiB-TC microcapsules can be caused by Si—O and B—O bonds.[17] However, this characteristic peak overlaps the FTIR spectrum of pure TC microcapsules, reducing its reliability. Fortunately, further evidences are provided by the X-ray photoelectron spectroscopy (XPS) result (Figure 2c; Figure S5, Supporting Information). Three characteristic peaks of pure TC microcapsules presented in 532.6, 398.4, and 285.7 eV are corresponding to O, N, and C elements, respectively (Figure S5a, Supporting Information). After being modified by APTES and boric acid, the signal intensity of the N element is significantly decreased, attributed to the shielding effect of the Si/B-containing shell.[18] Besides, the B and Si elements are presented (Figure S5b,c, Supporting Information). Through comparing the high-resolution XPS spectrum of N 1s in pure TC and SiB-TC microcapsules, a new peak near 401.5 eV is presented and may be caused by the ionization structure between amino and boric acid group (Figure 2-c_1; Figure S6, Supporting Information).[19] The influence of introducing a Si/B-containing shell in the thermochromic process is revealed by the Differential Scanning Calorimeter (DSC) curves (Figure 2-c2). During the heating process, fatty alcohol starts to melt by absorbing thermal energy, thus producing an endothermic peak from 15 to 30 °C.[20] The Si/B-containing shell does not change the process and temperature of the phase change of fatty alcohol, which determines the thermochromic function. As presented by transmission electron microscope (TEM) photographs (Figure S7a,b, Supporting Information), MMT and BN nanosheets demonstrate a typical layer structure, with particle sizes of 1.0 and 300 nm, respectively. A straight edge morphology is shown by MMT nanosheets, while BN nanosheets are circular. The different morphology characteristics in the TEM photographs of MMT and BN nanosheets are consistent with previous literature.[21]

The preparation process of PUA composite coating is presented in Figure 2d. The SiB-TC microcapsules, BN nanosheets, and MMT nanosheets are added to the polyether diamine precursor of PUA coating and the mixed suspension is stirred with the sonication for 2 h, thus obtaining a uniform dispersion. Then, the isocyanate curing agent is introduced to the above suspension to prepare PUA coating. Attributed to the appropriate viscosity, the PUA composite precursor can be processed onto the object's surface by both spray coating and blade coating (Figure 2d). The mechanical properties of pure PUA and PUA/SiB-TCM/BN/MMT (Blue) used as representative samples are also evaluated by tensile test (Figure S8, Supporting Information). In the initial stretching process, the stretching stress is rapidly increased to present a stress yield point of 9.6% and 10.0 MPa. Suffering from plastic deformation, pure PUA coating is fractured in elongation at beak of 154.0% and break strength of 9.3 MPa. With the addition of SiB-TCM, MMT, and BN nanosheets, the yield strength is significantly increased to 11.8 MPa. Meanwhile, the break strength of PUA/SiB-TC/BN/MMT (Blue) also increases to 11.9 MPa, with an improvement of 19.0% compared to pure PUA coating. A rising phenomenon is presented in the later plastic deformation process of PUA/SiB-TC/BN/MMT (Blue), may be attributed to the strong interfacial interactions between fillers and PUA resin. Therefore, it is also reasonable that the elongation at break of PUA/SiB-TC/BN/MMT (Blue) is reduced to 106.5%. Besides, the elongation at break of 106.5% and break strength of 11.9 MPa are able to support the practical application of the designed PUA composite coatings.

2.2. Solar Reflectance and Radiative Cooling Performance

Due to the phase change mechanism of fatty alcohol, the coupling and separation of the color former and color developer can be adjusted by the environment temperature. As a result, the PUA composite coatings with SiB-TC microcapsules are able to present customized colors at lower temperature (20 °C) and a light appearance at higher temperature (40 °C). As presented in Figure 2e, PUA composite coatings put onto the surface of the heating stage near 50 °C gradually lose their initial color and transition to a light appearance, attributed to the thermal melt of fatty alcohol. Cooling to room temperature, red, yellow, and blue colors can be shown again in PUA composite coating. After being heated at 80 °C for 7 days, the thermochromic performance of PUA composite coatings is studied. In an oven of 80 °C, the PUA composite coatings present a light appearance from beginning to end. Moving from the oven, the temperature of PUA composite coatings gradually decreases to room temperature, thus presenting a colored appearance. After being heated again, the light appearance is demonstrated again. The same result is shown in multiple cycles, indicating that the well cycle performance is not influenced by the long-time heat treatment (Figure S9, Supporting Information). Meanwhile, the solar reflectance spectra of PUA composite coatings are obtained by the UV–vis–NIR spectrophotometer (Figure 2f). At 20 °C, PUA composite coatings have selective absorption and reflection in the UV–vis region, corresponding to the characteristic color. When the test

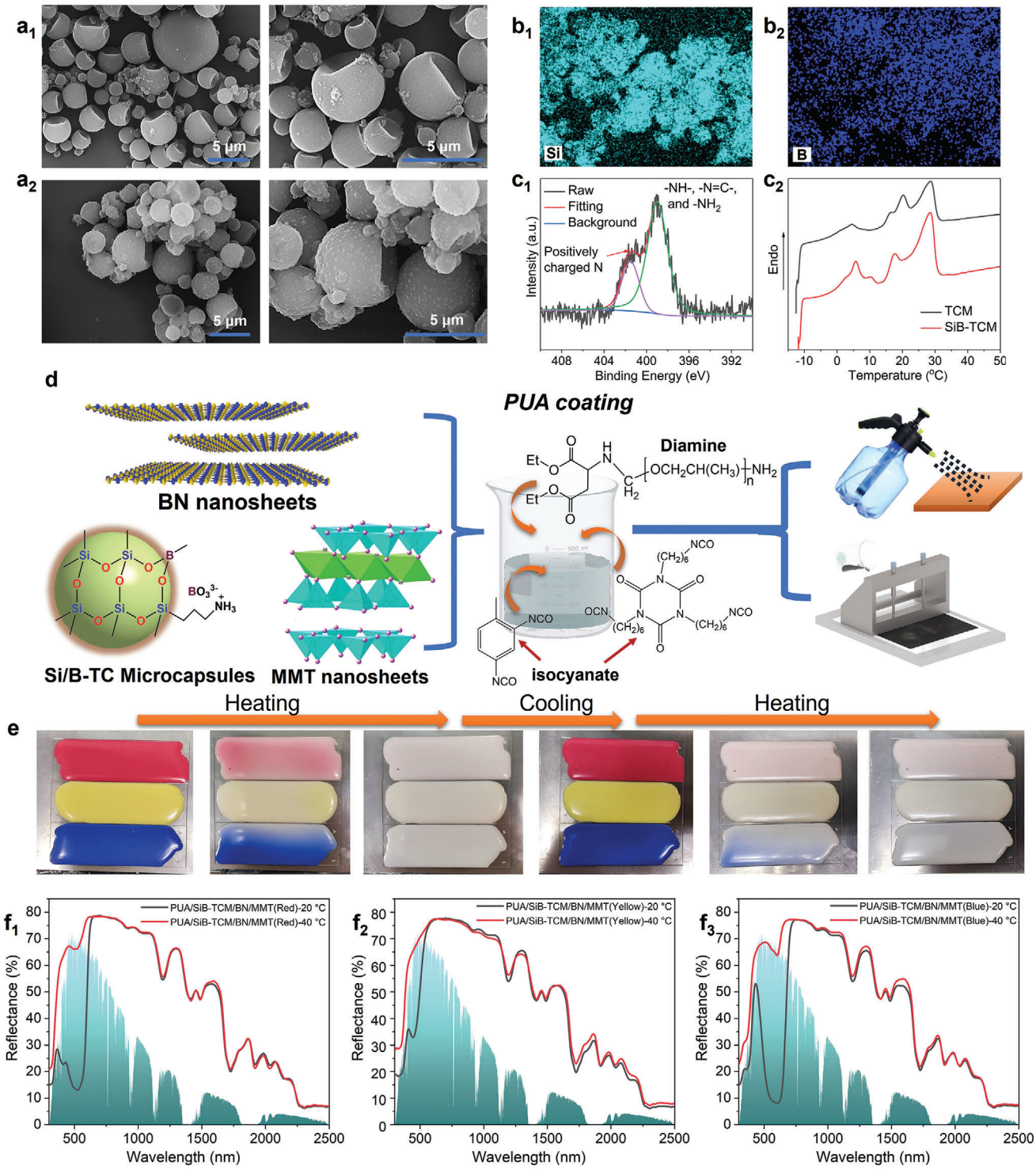

Figure 2. The preparation process and characteristics of PUA composite coatings. SEM images of pure TCM a_1) and SiB-TCM a_2) in different resolutions; SEM Mapping spectra of Si b_1) and B b_2) elements; c_1) High-resolution XPS spectrum of N 1s in SiB-TCM; c_2) DSC curves of pure TCM and SiB-TCM; d) Schematic for the preparation of PUA composite coatings; e) Thermochromic process of PUA/SiB-TCM/BN/MMT, corresponding to heating and cooling process; f_1–f_3) Reflectance spectra of PUA/SiB-TCM/BN/MMT at 20 and 40 °C, corresponding to red, white, and blue samples.

temperature receives 40 °C, the reflectivity of PUA composite coatings is increased, caused by the thermochromic process. According to Equation (1), the reflectivity in the UV–vis region and solar waveband PUA composite coatings can be calculated.[4]

$$r\ (\lambda,\theta,\varphi) = \int_{\lambda\min}^{\lambda\max} I_{solar(\lambda,\theta,\varphi)}\ r_{solar(\lambda,\theta,\varphi)} d\lambda \Big/ \int_{\lambda\min}^{\lambda\max} I_{solar(\lambda,\theta,\varphi)}\ d\lambda \quad (1)$$

where r is the reflection (%), λ is the wavelength (nm), λ_{min} and λ_{max} are minimum and maximum wavelength, respectively. θ is the polar angle, and φ is the azimuthal angle. $I_{solar}(\lambda)$ is the AM1.5G solar spectral irradiance at λ, and $r_{solar}(\lambda)$ is the light reflection (%) at λ. The reflectivity in the UV–vis region and solar waveband of PUA composite coatings is obviously increased (Table S1, Supporting Information). For example, the PUA/SiB-TCM/BN/MMT (Red) shows the reflectivity of 51.3% and 67.3% in the solar waveband, corresponding to 20 and 40 °C, respectively. The reflectivity in solar waveband of PUA/SiB-TCM/BN/MMT (Yellow) at 20 and 40 °C are 64.4% and 66.9%, while the reflectivity in solar waveband of PUA/SiB-TCM/BN/MMT (Blue) at 20 °C and 40°C are 46.1% and 65.3%. The reflectivity increase is mainly demonstrated in the UV–vis region, rather than the NIR region. Increasing to 40 °C from 20 °C, the thermochromic process results in increases of 27.8%, 9.6%, and 32.9% in reflectivity in the UV–vis waveband (Table S2, Supporting Information). Using PUA/SiB-TC/BN/MMT (Blue) as a representative sample, accelerated UV-light aging is performed to evaluate the resistance to aging of PUA composite coatings. After being illuminated by UV-light of 100 W/m^2 for 160 h, PUA/SiB-TC/BN/MMT (Blue) still present a well thermochromic function (Figure S10, Supporting Information). UV–visible-NIR spectrum is carried out to investigate the reflectivity change of PUA/SiB-TC/BN/MMT (Blue). It is found that the solar reflectivity of PUA/SiB-TC/BN/MMT (Blue) decreases to 43.6% from 46.1% at 20 °C (Figure S11, Supporting Information). However, the solar reflectivity at 40 °C is still kept at 64.6%, similar to the original samples (65.3%). Even though the solar reflectivity at 20 °C is decreased, this decrease is slight and further confirms its resistance to UV aging. It is found that the reflectivity of PUA composite coatings is still lower than those values reported by other literature dedicated to significantly increasing solar reflectivity. Fortunately, the thermochromic function successfully overcomes the contradictory relationship between aesthetic demand and solar reflectivity.[4]

$$\varepsilon\ (\lambda,\theta,\varphi)\ = \int_{\lambda\min}^{\lambda\max} I\ (\lambda,\theta,\varphi)\ \varepsilon\ (\lambda,\theta,\varphi)\, d\lambda \Big/ \int_{\lambda\min}^{\lambda\max} I\ (\lambda,\theta,\varphi)\, d\lambda \quad (2)$$

According to Equation (2), the emissivity of PUA composite coatings can be accurately obtained. The ϵ is the IR emissivity (%), λ is the wavelength (μm), λ_{min} and λ_{max} are 5 μm and 15 μm, respectively. θ is the polar angle and φ is the azimuthal angle. $I(\lambda)$ means the spectral intensity emitted by the blackbody at λ. Based on Equation (2), IR emissivity of pure PUA coating is ≈91.8%. As presented in **Figure** 3a and Table S3 (Supporting Information), the addition of TC microcapsules, SiB-TC microcapsules, BN nanosheets, and MMT nanosheets gradually increases the IR emissivity. The original spectrum file is provided by Supporting information. Interestingly, the emissivity is also influenced by the thermochromic process. The increasing test temperature effectively enhances the emissivity of PUA composite coatings at 5–15 μm (Figure 3b). At 20 °C, the overall IR emissivity of PUA/SiB-TCM/BN/MMT (Red), PUA/SiB-TCM/BN/MMT (Yellow), and PUA/SiB-TCM/BN/MMT (Blue) are 94.9%, 95.7%, and 96.1%, respectively. When the test temperature increases to 40 °C, the conjugate structure between color former and color developer is destroyed. Beyond expectation, the emissivity of PUA/SiB-TCM/BN/MMT (Red), PUA/SiB-TCM/BN/MMT (Yellow), and PUA/SiB-TCM/BN/MMT (Blue) is further increased to 98.0%, 96.9%, and 98.1%, respectively. The different IR emissivity in red, yellow, and blue PUA coatings can be interpreted by their chemical composition. For presenting different colors, 2′-chloro-6′-diethylaminofluoran, 3, 6-dimethoxyfluorane, and 6′-(diethylamino)−1′,2′-benzofluoran are used as the color former agents in red, yellow, and blue TC microcapsules, respectively. Obviously, the different chemical structures in color former agents will absorb their characteristic IR lights to cause different IR emissivities for red, yellow, and blue PUA coating samples, according to Kirchhoff's law. After being illuminated by UV-light of 100 W/m^2 for 160 h, IR emissivity of PUA/SiB-TC/BN/MMT (Blue) at 20 °C and 40 °C are 94.3% and 97.4%, respectively, which are extremely close to the original values (96.1% and 98.1%). Compared to previous most literature, this emissivity obtained is extremely high, presenting a huge potential to radiate the coatings' heat to outer space regarded as a cold source (**Table 1** and Figure 3c).[22–47]

According to Kirchhoff's law, IR emittance is equivalent to IR absorbance when an object is in thermodynamic equilibrium.[48] Therefore, IR emittance in the transparency atmospheric window is attributed to the IR characteristic absorption of chemical bonds, caused by symmetrical stretching, asymmetrical stretching, and bending vibration. The intensity of IR absorption is determined by the changing size of the dipole moment.[49] The dipole moment is formed during molecular vibrations, which is the product of the distance between the centers of positive and negative charges and the amount of charge at these centers. According to previous literature, the interfacial interactions and hydrogen-bond interactions can promote the inhomogeneous distribution of electric charge in chemical bonds, thus increasing the changing size of dipole moment during molecular vibrations.[12,50] Therefore, the high IR emissivity may be attributed to the strong interfacial interactions. To demonstrate this view, the interfacial interaction of PUA composite coatings is explained by first observing the fracture surface of PUA composite coatings. After being broken in liquid nitrogen, a relatively smooth surface with small swellings is presented for the fracture surface of pure PUA, indicating a brittle rupture phenomenon (Figure 3-d1).[51] In contrast, many circular protrusions and holes are uniformly dispersed in the fracture surface of PUA composite coatings, attributed to the incorporated SiB-TC microcapsules. The uniform distribution strongly confirms the well-dispersion state of SiB-TC microcapsules. Meanwhile, the fracture surface of PUA composite coatings becomes much rougher, even using liquid nitrogen to realize the brittle failure (Figure 3-d2). Compared to the molecule chain of PUA itself, the combination of BN nanosheets, MMT nanosheets, and SiB-TC microcapsules provides a more robust supporter to tolerate external stress. During the breakage process, the external stress could not straight pass through the test spline and suffered from a load transfer, thus forming a rough fracture

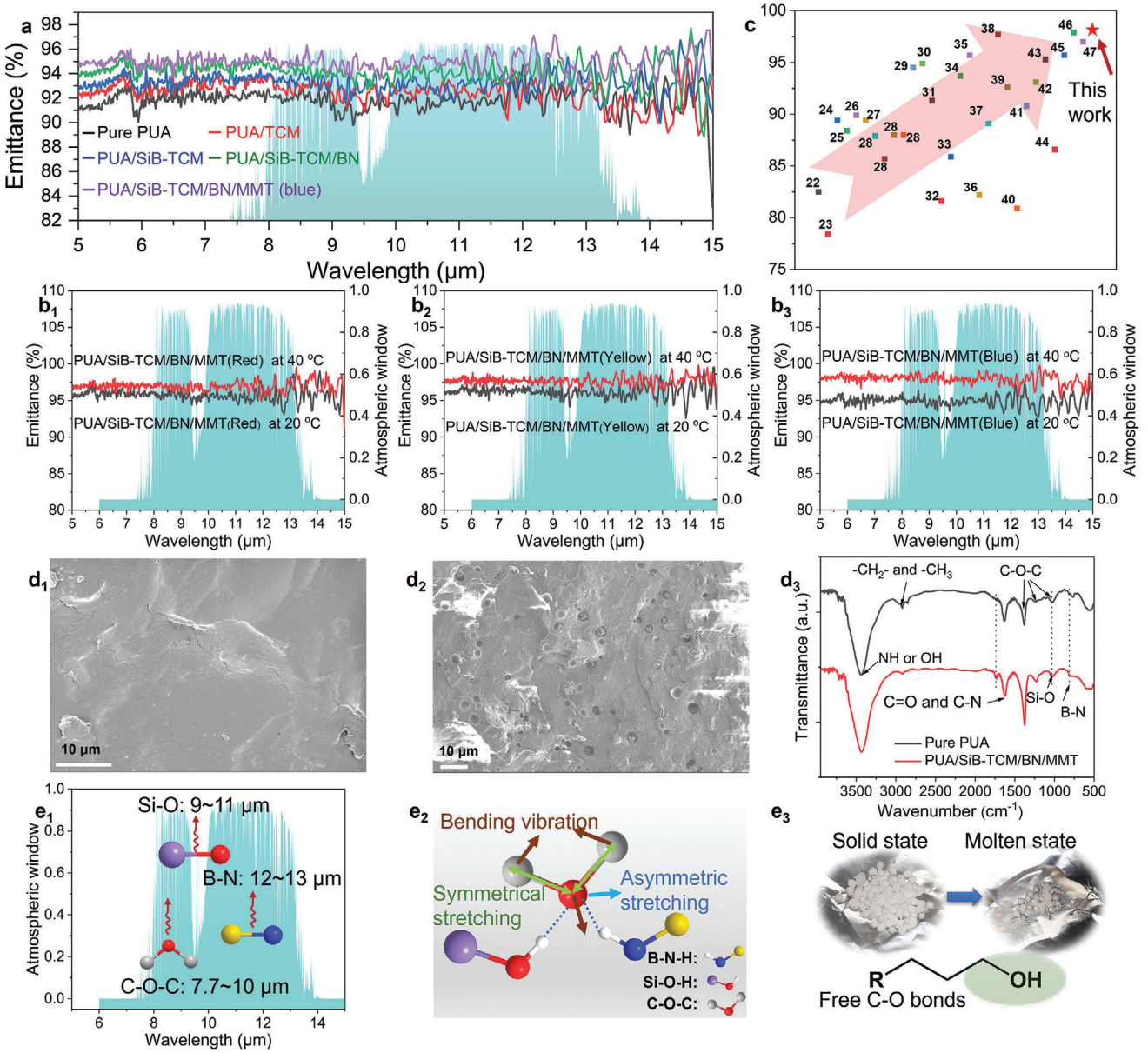

Figure 3. IR emissivity and mechanism of PUA composite coatings. a) IR emittance spectra of pure PUA and its composite coatings (Blue) at 5–15 μm; IR emittance spectra of PUA/SiB-TCM/BN/MMT at 20 and 40 °C, corresponding to red b_1), yellow b_2), and blue b_3) samples; c) The emissivity comparison of PUA/SiB-TCM/BN/MMT (Blue) at 40 °C with other research works; SEM images of fracture surface of d_1) pure PUA and d_2) PUA/SiB-TCM/BN/MMT (Blue); d_3) FTIR spectra of pure PUA and PUA/SiB-TCM/BN/MMT (Blue) coatings; Schematic for e_1) IR emission peak of C—O—C, Si—O, and B—N bonds in atmospheric window, e_2) Asymmetrical distribution of electric charge in C—O—C, B—N, and Si—O bonds, e_3) Switch of fatty alcohol between solid and melt to expose more C-O-H.

surface. This result strongly confirms the enhanced interfacial interaction between fillers and PUA resin.[51] In addition, FTIR spectra of pure PUA and its composite coatings are also performed to analyze the interfacial interaction, indicating similar FTIR spectra attributed to the same polymer matrix (Figure 3-d_3; Figure S13, Supporting Information). The characteristic peaks of pure PUA near 3439, 2917, and 1630 cm^{-1} are attributed to the vibration of N—H and O—H, —CH_2— and —CH_3, as well as C═O and C—N bonds, respectively. Moreover, the characteristic peaks of Si—O and B—N bonds overlap with the molecule structure of PUA resin.[52] A new peak near 1738 cm^{-1} in the FTIR spectrum of PUA/SiB-TCM/MMT/BN composite coating is due to the presence of MMT nanosheets, according to our previous work reporting FTIR spectra of BN and MMT nanosheets.[52,53] Most importantly, it is found that the characteristic peak from the N—H and O—H bonds of PUA/SiB-TCM/MMT/BN composite coating moves to 3429.9 cm^{-1} from 3439.3 cm^{-1}, demonstrating a red shift phenomenon may be caused by the hydrogen-bond interactions (Figure S13, Supporting Information). Based on the above results, the formation mechanism of extremely high IR

Table 1. Comparison result of IR emissivity.

Authors	Fabrication method	IR emissivity (%)	Product types
Chae et al.[22]	Electron beam evaporation	82.5	Film
Ma et al.[23]	Chemical vapor deposition	78.4	Film
Kou et al.[24]	Electron beam evaporation	89.4	Film
Zhou et al.[25]	Blade coating method	88.4	Film
Chae et al.[26]	Chemical vapor deposition	89.9	Film
Yang et al.[27]	Bridgman-stockbarger	89.4	Film
Bao et al.[28]	Spraying coating	87.9	Film
Bao et al.[28]	Spraying coating	85.7	Film
Bao et al.[28]	Spraying coating	88.0	Film
Bao et al.[28]	Spraying coating	88.0	Film
Meng et al.[29]	Coating and thermal annealing	94.5	Film
Kang et al.[30]	Dissolving and drying	94.9	Film, paint, coating
Tian et al.[31]	Air spraying	91.3	Film, paint, coating
Ao et al.[32]	Deposition, magnetron sputtering	81.6	Film
Banik et al.[33]	Electron beam evaporation, dip coating	85.9	Film
Jeong et al.[34]	Micro fabrication	93.7	Film
Zhang et al.[35]	Wet chemical etching	95.7	Film
Heo et al.[36]	Deposition electron beam evaporation	82.2	Film
Shi et al.[37]	Natural materials	89.1	N/A
Wu et al.[38]	microfabrication	97.7	Film
Zhai et al.[39]	Roll-to-roll manufacturing	92.6	Film
Zhao et al.[40]	Roll-to-roll manufacturing	80.9	Film
Huang et al.[41]	Dissolving in solution and mixing, drying	90.8	Film, paint, coating
Li et al.[42]	Mixing and coating	93.1	Film, paint, coating
Li et al.[43]	Mixing and coating	95.3	Film, paint, coating
Liu et al.[44]	Fast photo-polymerization	86.6	Film
Xue et al.[45]	Mixing, stirring, painted	95.7	Film, paint, coating
Meng et al.[46]	Block copolymer	97.9	Film
Cai et al.[47]	Ball Milling	97.0	Cellulose Metamaterials
PUA/SiB-TCM/BN/MMT (Red)	Spaying, coating	98.0 (40 °C)and 94.9 (20 °C)	Film, paint, coating
PUA/SiB-TCM/BN/MMT (Yellow)	Spaying, coating	96.9 (40 °C) and 95.7 (20 °C)	Film, paint, coating
PUA/SiB-TCM/BN/MMT (Blue)	Spaying, coating	98.1 (40 °C) and 96.1 (20 °C)	Film, paint, coating

emissivity can be speculated: First, C—O—C (7.7–10 μm), B—N (12–13 μm), and Si—O (9–11 μm) bonds have characteristic IR emission in the transparency atmospheric window (Figure 3-e1).[5,13] The carbamido group in PUA molecules also provides strong hydrogen-bond interactions to C—O—C bonds, thus establishing the intrinsic IR emissivity of up to 91.8%. Second, the strong interfacial interactions among PUA resin, BN nanosheets, and MMT nanosheets promote the inhomogeneous distribution of electric charge in C—O—C, B—N, and Si—O bonds, thus improving the change of dipole moment (Figure 3-e2). The changing dipole moment further improves the energy levels generated by molecular vibrations including bending and asymmetric modes, to producing more IR emission. Third, in the molten state, the free C-O bonds in fatty alcohol is capable of absorbing more IR radiation (Figure 3-e3). As a result, the IR emissivity much higher than other research works is mainly attributed to three reasons: existence of C—O—C, Si—O, and B—N bonds, strong interfacial interactions, and free C-O bonds in molten fatty alcohol.

For validating the passive radiative cooling effect of PUA composite coatings, a homemade detecting platform is used to record the temperatures, humidity, and solar intensity (**Figure 4a**). First, the PUA composite coatings and their control samples covered by the polyethylene (PE) film are put onto the top of polystyrene (PS) foam, which is packaged by aluminum foil. The composition of control samples is the same with the PUA composite coating, except for SiB-TC microcapsules treated by the ethyl alcohol solution with pH = 1. Due to the removal of fatty alcohol, SiB-TC microcapsules lose their thermochromic function. Second, the bottom temperatures of six samples are also detected by the thermocouples. Meanwhile, the distance between samples and thermocouples is 5.0 cm. Third, the meteorological station

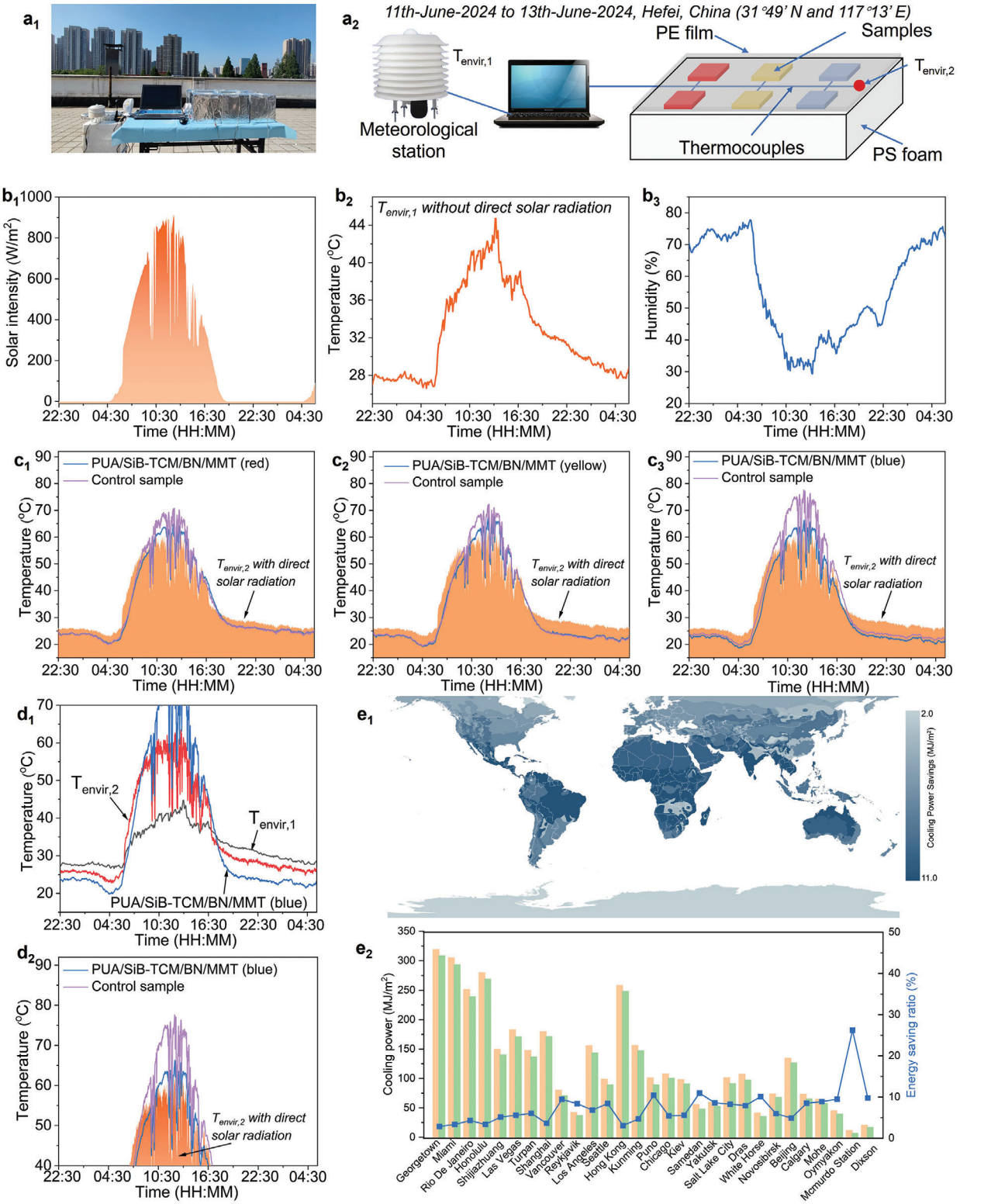

Figure 4. Radiative cooling performance and Energyplus simulation. Digital photo a_1) and a_2) schematic for the radiative cooling test, monitoring importantly two environment temperatures provided by the meteorological station and thermocouples; Solar intensity b_1), environment temperature b_2), and humidity b_3) during the test; c_1–c_3) Temperature curves of PUA composite coatings and their control samples; d_1) Temperature curves at nighttime of PUA/SiB-TCM/BN/MMT (Blue), control sample, and $T_{envir,2}$; d_2) Temperature curves at daytime of PUA/SiB-TCM/BN/MMT (Blue), control sample, and $T_{envir,2}$; e_1) Energy-saving performance on a worldwide scale considering the energy consumed by cooling systems, fans, and heating equipment; e_2) Energy saving in representative cities for 28 climate regions.

collects the environment humidity, solar intensity, and first environment temperature ($T_{envir,1}$). In addition, the temperature located between PE film and PS foam is also recorded, regarded as the second environment temperature ($T_{envir,2}$). Obviously, the $T_{envir,1}$ provided by the meteorological station not only considers the heat convection and transfer but also successfully avoids the direct solar radiation, while $T_{envir,2}$ only considers the radiative interchange approach of heat. There are numerous reports of chaotically using the above two temperatures as ambient temperatures, causing great confusion. In fact, the temperature test method provided by the meteorological observatory is similar to $T_{envir,1}$, requiring the conditions of keeping out of the sun and ventilation. Obviously, the two environment temperatures used in this work can significantly enhance the reliability of the field test, further explaining the passive cooling performance in complicated outdoor environments.[4] The test date is recorded from 22:30 11th-June-2024 to 04:30 13th-June-2024, and the test location is Hefei City, China (31°49′ N and 117°13′ E).

In accord with the order of nature, on 12th June 2024, the solar intensity suffers from a first gradually increasing and then gradually decreasing process (Figure 4-b1). Meanwhile, the highest solar intensity on the 12th day is 902 W/m^2. The well sunshine condition provides an appropriate test environment for the radiative cooling performance. $T_{envir,1}$ tested by the meteorological station corresponds to the natural law of solar intensity, up to 44.7 °C (Figure 4-b2). Interestingly, $T_{envir,1}$ is rapidly increased with the sunrise and slowly reduced during sunset and night. This phenomenon not only indicates the large amount of heat brought by solar illumination but also confirms the heat preservation effect of the atmosphere. The ambient humidity simultaneously recorded by the meteorological station demonstrates an opposite trend, in contrast to the environment temperature (Figure 4-b3). Figure 4c demonstrates the temperature curves of six samples and $T_{envir,2}$. Attributed to the direct solar radiation, $T_{envir,2}$ in the daytime is much higher than $T_{envir,1}$, as presented in Figure 4-d1. However, in the nighttime, the heat convection and transfer cause a higher temperature in the $T_{envir,1}$. In the nighttime, it is worth noting that the temperatures of PUA composite coatings and control samples are obviously lower than $T_{envir,2}$, attributed to the passive radiative cooling effect. Compared with $T_{envir,2}$, the maximum temperature decrease is presented by the PUA/SiB-TCM/BN/MMT (Blue), an average value of ≈5.8 °C in the nighttime from 22:30 12th-June-2024 to 04:30 13th-June-2024 (Figure 4-d1). In addition, a more significant decrease (≈7.6 °C) is presented in the same time, compared with $T_{envir,1}$ (Figure 4-d1). Meanwhile, compared with $T_{envir,1}$, average sub-ambient temperatures in nighttime of ≈6.6 and ≈4.1 °C are also demonstrated in PUA/SiB-TCM/BN/MMT (Yellow) and PUA/SiB-TCM/BN/MMT (Red). This result is strongly according to the emissivity results, which confirm the emissivity of 94.9%, 95.7%, and 96.1% in PUA/SiB-TCM/BN/MMT composite coatings (Figure 3b). In fact, most of the time, $T_{envir,2}$ is higher than temperatures of PUA/SiB-TCM/BN/MMT composite coatings and control samples. Only with high solar intensity, the temperature of control samples and PUA composite coatings are much higher than $T_{envir,2}$, as presented in Figure 4c. Beyond all doubt, the higher temperatures in control samples and PUA composite coatings are attributed to the solar absorption and heating effect. In other words, the high reflectivity is the fundamental condition of the daytime radiative cooling. However, this work is dedicated to balancing the radiative cooling and aesthetic demand, rather than solely pursuing the extremely high reflectivity causing a monotonous color world.

There is an interesting phenomenon that the highest temperature is presented by the control sample with blue color, attributed to the reflection in the blue waveband and absorption in the other waveband. The blue appearance indicates that other visible light such as red and yellow solar light is absorbed, which occupy dominating solar energy.[54] Compared to the control sample (Blue), the maximum temperature reduction in PUA/SiB-TCM/BN/MMT (Blue) is up to ≈16.7 °C. Meanwhile, the maximum temperature decreases of ≈7.3 and ≈5.8 °C are also demonstrated by PUA/SiB-TCM/BN/MMT (Red) and PUA/SiB-TCM/BN/MMT (Yellow). Due to the failed thermochromic function caused by the removal of fatty alcohol, the control samples still present a colored appearance to absorb the solar radiation and further increase the materials' temperatures. Higher than the solar intensity of 500 W m^{-2}, the average temperature decreases of ≈3.6, ≈3.3°C, and ≈8.3°C, are presented in PUA/SiB-TCM/BN/MMT (Red), PUA/SiB-TCM/BN/MMT (Yellow), PUA/SiB-TCM/BN/MMT (Blue), respectively, compared to control samples. The different radiative cooling efficiencies in PUA composite coatings are also interpreted. In the daytime, even though the thermochromic process is demonstrated for PUA composite coatings (as presented in Figure 2e), the pure white appearance is not shown and solar light is still absorbed in the visible region. As presented in Figure 2f and Table S1 (Supporting Information), the solar absorptivity of red, yellow, and blue PUA composite coatings is different, indicating a different solar heating effect. Different radiative cooling efficiencies in the daytime are mainly attributed to the differentiated absorption in solar waveband. In addition, in the nighttime, the solar heating effect is avoided and the IR emissivity determines the radiative cooling efficiency. Based on the different IR emissivity (Figure 3b), it is also reasonable that red, yellow, and blue samples present different radiative cooling efficiencies in the nighttime. Therefore, the designed PUA composite coatings not only significantly radiate the material's heat to outer space by the high IR emissivity but also effectively reduce the solar absorption daytime with the thermochromic function.

The energy consumption in building cooling is further simulated by the *EnergyPlus* software. The building model is presented in Figure S14 (Supporting Information) and uploaded as Supporting Materials. It is hypothesized that the building surface is covered by PUA/SiB-TCM/BN/MMT (Blue) coating and its control sample treated by ethyl alcohol solution. The detailed parameters of coatings are provided in the Experimental Part. The earth is covered by twenty-eight climates, including tropical rainy climate, tropical monsoon climate, and so on (Presented in Table S4, Supporting Information). Directing at each climate, 28 representative cities and regions are employed (Table S4, Supporting Information). Based on the building model, it is found that the employment of PUA/SiB-TCM/BN/MMT (Blue) coating brings effective decreases in cooling power, from 2.02 to 10.76 MJ m^{-2} (Figure 4-e1). Meanwhile, a decrease of near 10.0 MJ m^{-2} in cooling power is demonstrated in Miami, Rio de Janeiro, Las Vegas, Los Angeles, and Puno, corresponding to tropical monsoon climate, tropical savanna climate, tropical desert climate,

Mediterranean climate, and tropical monsoon climate (very dry winters). Besides, the decrease ratios are more significant in the cooling power of Vancouver, Puno, Samedan, and White Horse, for marine subtropical humid climate, tropical monsoon climate (very dry winters), humid continental climate (extremely cold winters), continental grassland climate (hot summers, extremely cold winters). Interestingly, the largest reduction ratio is presented for McMurdo Station, of which the population is very small. Meeting the aesthetic demand, this simulation result strongly confirms the potential of thermochromic and highly IR-emissive composite coating to decrease the energy consumption of building cooling worldwide.

2.3. Fire Safety Performance and Its Mechanism Analysis

Generally speaking, the approach toward decreasing the energy consumption in building cooling mainly focuses on the exterior wall coatings.[55] Due to its organic composition including C, N, O, and H elements, the exterior wall coatings are easily ignited and further release heat and toxic gases.[56] Even worse, the high temperature brought by the combustion of the exterior wall coatings will further cause fire propagation. This work is dedicated to developing thermochromic and passive radiative cooling polymer-based coatings that are applied as exterior wall coatings, thus decreasing the energy consumption in building cooling. Therefore, the fire safety performance is significantly important for the coatings we designed. Herein, a series of test measurements is carried out to investigate the fire safety performance of PUA composite coatings with blue appearance. The thermogravimetric analysis (TGA) results under nitrogen atmosphere of PUA composite coatings are presented in Figure S15a (Supporting Information). The temperature corresponding to 5 wt.% loss ($T_{5\ wt.\%}$) is regarded as the initial decomposition temperature. It is found that the $T_{5\ wt.\%}$ of pure PUA is 287.6 °C, while the addition of TC microcapsules (4.0 wt.%), SiB-TC microcapsules (4.0 wt.%), BN nanosheets (1.0 wt.%), and MMT nanosheets (4.0 wt.%) slightly decreases the $T_{5\ wt.\%}$ (Table S5, Supporting Information). A more obvious decrease in mass loss is presented from 300 to 500 °C, mainly attributed to the low thermal stability of fatty alcohol in TC and SiB-TC microcapsules.[57] Fortunately, a significant increase in char residue over 500 °C of PUA composite coatings is observed, indicating the high char-forming ability (Figure S15b, Supporting Information). The incorporation of pure TC microcapsules does not increase the char residue over 500 °C, while the mass loss from 300 to 500 °C is largest compared to other samples. Compared to PUA/TCM composite coatings, the Si/B-containing shell contributes to reducing the mass loss from 300 to 500 °C of PUA/SiB-TCM. Besides, char residue at 600 °C is increased to 6.1 wt.% from 2.2 wt.%. Incorporating 1.0 wt.% BN nanosheets into PUA composite coating also does not effectively increase the char residue at 600 °C. The slight increase in PUA/SiB-TCM/BN is the intrinsic mass of BN nanosheets with high thermal stability. Surprisingly, 4.0 wt.% MMT nanosheets significantly increase the char residue at 600 °C to 13.6 wt.% from 2.2 wt.%. The above results indicate that the pure TC microcapsules will decrease the thermal stability and BN nanosheets do not effectively promote the char formation. The enhanced thermal stability is mainly attributed to the Si/B-containing shell and MMT nanosheets, which will be thermally molten to form a protective layer.[58] Micro calorimeter test (MCC) is developed to analyze the heat release from the combustion of pyrolysis products under a nitrogen atmosphere (Figure S16 and Table S6, Supporting Information). There are three peaks in the heat release curves of PUA composite coatings, corresponding to different pyrolysis stages (Figure S16a, Supporting Information). Compared to pure PUA coating, the peak value in the first stage of PUA composite coatings is increased. Besides, the largest value of heat release rate (HRR) in pure PUA coating is up to 174.5 W g^{-1}, presented in the third stage. However, the largest value of HRR in PUA composite coatings is presented in the second stage. These results are consistent with the TGA data under a nitrogen atmosphere, including mass loss from 300 to 500 °C and char residue over 500 °C. As expected, the corporating addition of SiB-TC microcapsules, BN nanosheets, and MMT nanosheets effectively decrease the peak value of HRR in the second and third pyrolysis stages, reduced by 16.4% and 29.5% compared with pure PUA (Figure S16b, Supporting Information). Different from the heat release rate, the total heat release obtained by the MCC test demonstrates that a significant decrease is realized only with the incorporation of MMT nanosheets.

However, the above measurements including TGA and MCC analysis are still small-scale methods. The fire ignition and propagation are speedy and vigorous. The small-scale means do not objectively evaluate the fire safety performance of PUA composite coatings.[59] The cone calorimeter test is used to further analyze the flame retardancy of SiB-TCM, BN nanosheets, and MMT nanosheets in the fire hazards of PUA composite coatings, by investigating heat release rate (HRR), total heat release (THR), CO release rate, total CO release, CO_2 release rate, and total CO_2 release. As presented in **Figure 5**-a1 and Table S7 (Supporting Information), the signal of heat release rate happens at 23 s and rapidly increases the peak value of HRR (PHRR) to 540.4 kW m^{-2} at 62 s. It is noteworthy that a response time of ≈3 s is needed for the signal identification. Therefore, the time to ignition of pure PUA coating is 20 s. The addition of pure TC microcapsules not only decreases the time to ignition but also increases the PHRR to 586.5 kW m^{-2}, mainly attributed to the low thermal stability and flammability of fatty alcohol. After introducing a Si/B-containing shell, the fire safety of PUA/SiB-TCM composite coatings is slightly enhanced, confirmed by the PHRR of 507.8 kW m^{-2}. The significant decrease in heat release rate is presented in PUA/SiB-TCM/BN and PUA/SiB-TCM/BN/MMT, showing PHRR values of 394.0 and 353.8 kW m^{-2}, reduced by 27.1% and 34.5%, respectively. Compared to the sharp curves in other samples, the HRR curves of PUA/SiB-TCM/BN and PUA/SiB-TCM/BN/MMT are much broader, confirming a suppressed heat release behavior. Meanwhile, the time to ignition is effectively prolonged to 31 s from 18 s. The effective suppression in the heat release rate may be attributed to the formation of a ceramic protective layer. Compared to the significantly decreasing HRR, the synergistic addition of SiB-TCM, BN nanosheets, and MMT nanosheets does not present a significant suppression effect in the total heat release (Figure 5-a2). The THR of pure PUA and PUA/SiB-TCM/BN/MMT are 33.2 and 28.6 MJ m^{-2}. The slight decrease (13.9%) in total heat release indicates that the incorporation of SiB-TCM, BN nanosheets, and MMT nanosheets

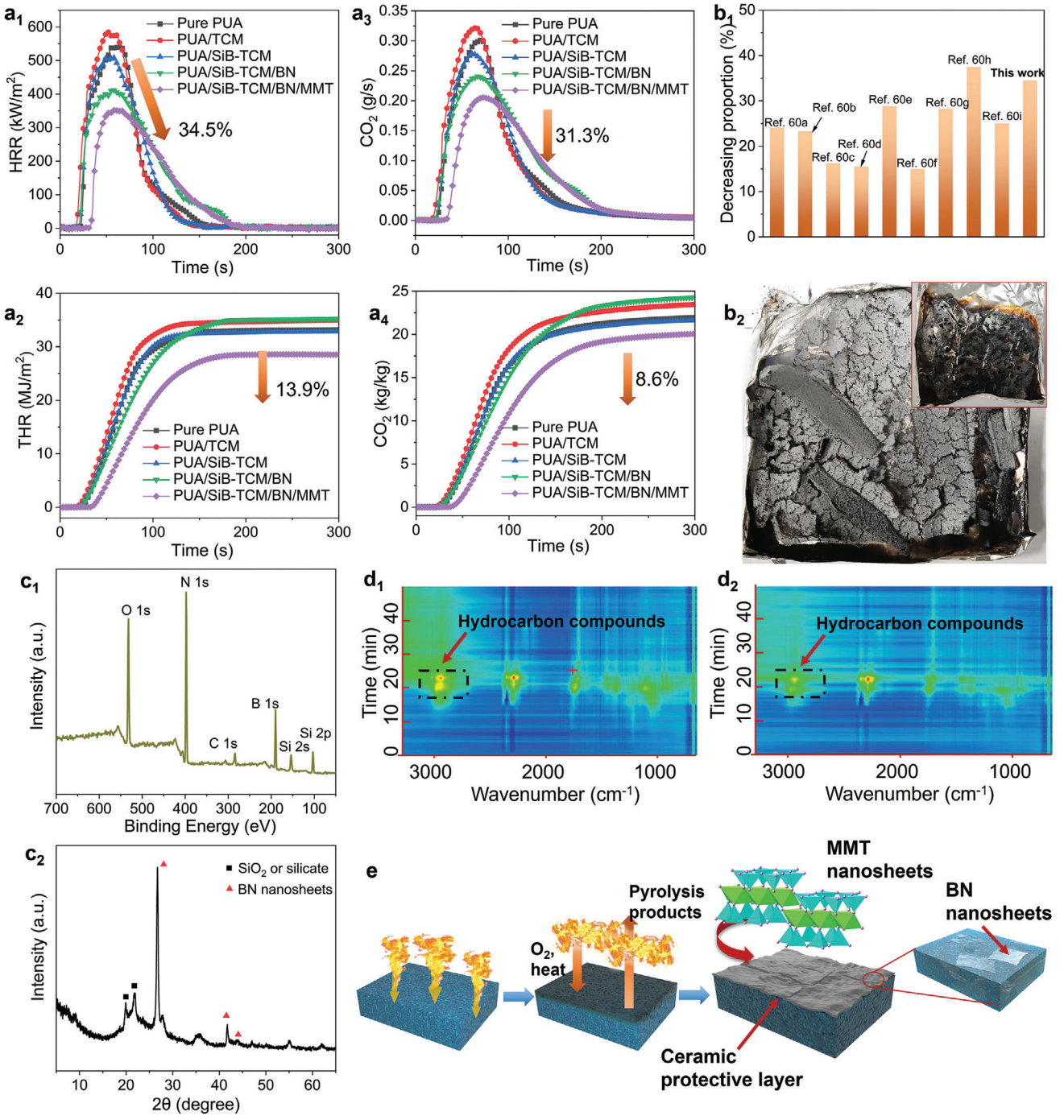

Figure 5. Fire safety performance and mechanism analyses, using blue samples as representative. HRR a_1), THR a_2), CO_2 release rate a_3), total CO_2 release a_4) curves of PUA composite coatings; b_1) Comparison result of flame retardancy of PUA composite coatings with other research works; b_2) Digital photos of char residue of PUA/SiB-TCM/BN/MMT composite coating (inset for pure PUA); XPS c_1) and XRD c_2) spectra of char residue of PUA/SiB-TCM/BN/MMT composite coating; e) Top view for the TG-IR spectra of pure PUA and PUA/SiB-TCM/BN/MMT composite coating.

effectively delays the combustion reaction, rather than reduces or changes the total combust consumption. The suppression effect of SiB-TCM, BN nanosheets, and MMT nanosheets in the PHRR of PUA resin are also compared with other research works reporting the flame retardancy of PUA resin (Figure 5-b1).[60] As a waterproof material, the polyether structure in the soft segment of PUA is crucial for avoiding the hydrolyzation of molecule chains. However, this polyether soft segment isn't conducive to the formation of char residue, which causes a huge challenge in improving the flame retardancy of PUA resin. Therefore, the decreasing ratio in PHRR of PUA resin is not significant, as reported by most literature. Fortunately, as reported by our work, the ceramic

protective layer formed by MMT nanosheets with the ceramization mechanism effectively hinders the combustion behavior of PUA resin to decrease PHRR value, superior to most research works.[60]

In addition, the release behavior of CO and CO_2 are also recorded to investigate the fire hazards of PUA composite coatings. Pure PUA coating and PUA/TCM composite coating present high CO release rates, near 0.0041 and 0.0046 g s^{-1} (Figure S17 and Table S8, Supporting Information). It is found that the maximum release rates of CO are approximate in PUA/SiB-TCM, PUA/SiB-TCM/BN, and PUA/SiB-TCM/BN/MMT. However, the slight but effective decrease in total CO release only be presented in PUA/SiB-TCM and PUA/SiB-TCM/BN composite coatings. Meanwhile, more CO is produced by PUA/SiB-TCM/BN/MMT, near 0.286 kg kg^{-1}. The release rule of toxic CO gas is very complicated, because both suppressed combustion and promoted combustion will bring more CO gas. Herein, the slightly increasing CO gas is attributed to the effective suppression of SiB-TC microcapsules, BN nanosheets, and MMT nanosheets in the combustion process of PUA composite coatings. In general, the release behavior of CO_2 is the same to the combustion heat, because of the conservation rule of mass and energy. As expected, the overall trend of CO_2 curves is similar to the HRR curves (Figure 5-a3). The maximum CO_2 release rate is up to 0.327 g s^{-1}, presented by PUA/TCM. Obviously, the highly flammable TC microcapsules mainly composed of fatty alcohol will increase the fire hazards of PUA composite coatings. Compared to pure PUA coating, the modification of Si/B-containing shell, BN nanosheets, and MMT nanosheets effectively decreases the CO_2 release rate. Meanwhile, a CO_2 release rate of low to 0.204 g s^{-1} is presented in PUA/SiB-TCM/BN/MMT, decreased by 31.3%. However, the total CO_2 release is slightly decreased by 8.6%, indicating a similar mass combusted in all samples (Figure 5-a_4). Therefore, the synergistic system composed of SiB-TCM, BN nanosheets, and MMT nanosheets mainly put off the heat release process, rather than reducing the total release amount. There are two indexes to evaluate the fire hazards, i.e., fire propagation index (FPI) and fire growth index (FGI). FPI is defined as the ratio of time to ignition (TTI) to PHRR, which reflects the flame resistance of the material after ignition. The larger FPI value represents a lower fire hazard. FGI is defined as the ratio of PHRR to time corresponding to PHRR, representing the spread rate of fire. Compared with pure PUA, the synergistic system composed of SiB-TCM, BN nanosheets, and MMT nanosheets not only increases FPI to 0.088 from 0.037, but also decreases FGI to 6.00 from 6.65 (Table S6, Supporting Information). In other words, both fire growth rate and fire propagation rate are significantly hindered, attributed to the formation of a ceramic protective layer.

2.4. Fire Safety Mechanism Analysis

After being burned with the cone calorimeter test, pure PUA and its composite coatings left different char residues, in terms of yield and morphology. As presented in the inset of Figure 5-b2, little and fragmentary char residue is left during the PUA combustion. The char residue in PUA/TCM and PUA/SiB-TCM is not changed, corresponding to the cone calorimeter result (Figure S18a,b, Supporting Information). Meanwhile, the further incorporation of BN nanosheets significantly increases the char residue (Figure S18c, Supporting Information). In view of the extremely high thermal stability, BN nanosheets do not directly participate in the formation of char residue. Therefore, it is more likely that BN nanosheets present a barrier effect to promote the formation of char residue. More importantly, incorporating MMT nanosheets into the synergistic system produces an intact, continuous, and gray char residue (Figure 5-b2). The gray appearance is due to the production of silicate from MMT nanosheets, at high temperatures. Obviously, the addition of MMT nanosheets is the most essential reason for the enhanced fire safety performance.

The char residue of PUA/SiB-TCM/BN/MMT is further analyzed by the XPS spectrum, thus revealing the element composition (Figure 5-c1). The elements constituting the char residue include C, N, O, B, and Si. It is an interesting phenomenon that the weight ratio of C is much lower than B, N, and O. However, as reported by previous literature, the main element of char residue should be carbon.[61] This different result is attributed to the discrepant flame retardancy mechanism. The high-resolution XPS spectra of Si 2p and O 1s are demonstrated in Figure S19 (Supporting Information). The binding energy located at 103.4 eV and 102.5 eV are corresponding to Si—O and Si—C bonds. Meanwhile, the O element participates in the formation of char residue with forms of O—C, O—B, and O—Si bonds.[17] The crystal structure of char residue in PUA/SiB-TCM/BN/MMT is also studied by X-ray diffraction (XRD) spectrum (Figure 5-c_2). The characteristic peaks near 26.7°, 41.6°, and 43.9°, are attributed to the (002), (100), and (101) planes of BN nanosheets.[62] Besides, converting MMT nanosheets to SiO_2 or silicate also brings the characteristic peaks located at 19.8° and 21.7°. The characteristic peaks related to diboron trioxide, usually locating at 26.0°, 32.2°, 40.4°, and 43.1°, are not found. As reported by previous literature,[63] the boric acid or boric oxide bond is usually used to improve the strength and compactness of ceramics. Their structure is regarded as a 2D network composed of boron-oxygen triangles ([BO_3]), which can transform to boron-oxygen tetrahedron ([BO_4]) above 400 °C. Especially, during the high-temperature environment caused by the combustion, [BO_4] can combine with the silicon-oxygen network to form Si—O-B structure and improve the compactness and strength of ceramics. Therefore, the boron element may take part in the formation of a protective ceramic layer, rather than synthesizing the diboron trioxide.

The thermogravimetric analysis/infrared spectrometry coupling technique (TG-IR) is performed to investigate the gaseous pyrolysis products of pure PUA and PUA/SiB-TCM/BN/MMT coatings. The 3D views of the characteristic peak and intensity of pyrolysis products are presented in Figure S20 (Supporting Information). However, the scale in vertical coordinates of pure PUA and PUA/SiB-TCM/BN/MMT is not the same. Therefore, it is not able to compare the peak intensity directly. Besides, the wavenumber of characteristic peaks in pure PUA and PUA/SiB-TCM/BN/MMT is highly coincident, confirming the same pyrolysis products. The characteristic peaks near 2934, 2283, 1712, and 1457 cm^{-1} are attributed to the generation and release of hydrocarbons, CO_2, carbonyl, and aromatic, respectively (Figure S21a, Supporting Information).[64] Shown by the top view (Figure 5-d1,d_2), the signal intensity of characteristic peak corresponding to hydrocarbon compounds in

PUA/SiB-TCM/BN/MMT is decreased, compared with pure PUA. After being homogenized by the sample mass, the signal intensity of characteristic peaks is compared directly to investigate the release behavior of gaseous pyrolysis products (Figure S21b–f, Supporting Information). Obviously, the decreasing intensity in all characteristic peaks indicates that less pyrolysis products are released. In fact, the TG-IR spectrum is also carried out at nitrogen atmosphere, same to the TGA and MCC tests performed in this work.

In sum, the more residue in the TGA result, less heat release in the MCC test, and less gaseous pyrolysis products in TG-IR spectra strongly confirm that the addition of SiB-TCM, BN nanosheets, and MMT nanosheets effectively enhance the thermal stability and suppress the generation of gaseous pyrolysis products. Even though TC microcapsules will increase the fire hazards, the Si/B-containing shell will counteract the side effects of the fatty alcohol of TC microcapsules. Meanwhile, the morphology and element composition in the residue of PUA/SiB-TCM/BN/MMT after the cone calorimeter test indicates that a ceramic protective layer is formed, rather than the carbonaceous residue. In addition, the XRD spectra of PUA/SiB-TCM/BN/MMT residue also demonstrate that BN nanosheets do not participate in the formation of a ceramic protective layer but enhance the mechanical robustness. The credible flame retardancy mechanism is presented in Figure 5e. During combustion, the heat, oxygen, and pyrolysis products will be delivered between PUA coating and fire. Meanwhile, MMT nanosheets will be melted at high temperatures to form a molten protective layer for suppressing the exchange of heat and mass. In the whole process, BN nanosheets not only synergistically present a barrier effect to suppress the exchange of heat and mass, but also enhance the mechanical robustness of the melting and ceramic protective layer.

3. Conclusion

In this study, we successfully developed a thermochromic, extremely-high IR emissive, and flame-retardant PUA composite coating to effectively reduce energy consumption in building cooling while meeting the aesthetic demand and enhancing the fire safety performance. Utilizing commercial thermochromic (TC) microcapsules as the core material, a Si/B-containing shell was synthesized on the microcapsule surface using TEOS, APTES, and boric acid as precursors. Additionally, SiB-TC microcapsules were combined with BN and MMT nanosheets and incorporated into the PUA composite coating using a solvent-free approach. Inspired by the chameleon, the thermochromic function of the PUA composite coatings allows them to switch from red, yellow, and blue to light appearance, resulting in increases of 27.8%, 9.6%, and 32.9% in the reflectivity of UV–vis waveband. Correspondingly, the IR emissivity of PUA/SiB-TCM/BN/MMT (Red), PUA/SiB-TCM/BN/MMT (Yellow), and PUA/SiB-TCM/BN/MMT (Blue) increase to 98.0%, 96.9%, and 98.1% from 94.9%, 95.7%, and 96.1%, when the temperature rises from 20 to 40 °C. During hot daytime conditions, compared to control samples without the thermochromic function, the PUA/SiB-TCM/BN/MMT composite coatings achieve average temperature reductions of approximately ≈3.6, ≈3.3, and ≈8.3 °C for red, yellow, and blue colors, respectively. At night, the extremely high IR emissivity results in average sub-ambient temperatures of ≈7.6, ≈6.6, and ≈4.1 °C in the corresponding samples, compared to $T_{envir,1}$. *EnergyPlus* simulations indicate that the combination of thermochromic function and extremely high emissivity is applicable in most regions worldwide. More importantly, the synergistic system of SiB-TCM, BN nanosheets, and MMT nanosheets contributes to the formation of a ceramic protective layer, which mitigates the fire hazards of the designed PUA composite coatings. Along with the solvent-free method, the enhanced fire safety performance, thermochromic function, and high IR emissivity collectively promote the practical application of radiative cooling materials, significantly reducing energy consumption in building cooling.

4. Experimental Section

Raw Materials: Commercial TC microcapsules are provided by the Shuer Chemical Co., Ltd. (Wuhan, China). APTES, TEOS, and boric acid are purchased from Sinopharm Chemical Reagent Co., Ltd. BN powder is offered by Aladdin Industrial Co., Ltd. (Shanghai, China), of which the average particle size was ≈1 µm. MMT powder (sodium-intercalated, K-10) with a surface area of 240 m^2 g^{-1} is supported by Macklin Industrial Co., Ltd. (China). PUA coating (N-100) was provided by Feiyang Polyurea Co., Ltd (Shenzhen, China), using aspartame polyurea and crosslinking structures. In addition, organic solvent is not used here and only deionized water is consumed.

Synthesis of SiB-TC Microcapsules: The 1.0 g commercial TC microcapsules (red, yellow, and blue) were first added to 100 mL deionized water and then the microcapsules were uniformly dispersed by the mechanical stir and sonication for 2 h. Further, the sonication was tuned out and 0.5 g TEOS was introduced to the above mixture. Due to its insoluble characteristic in water, TEOS will gather onto the surface of TC microcapsules. Then, 0.1 g APTES added can trigger the sol-gel reaction of TEOS to produce a Si—O network, with hydroxyl ions from the ionization reaction of water. After the reaction of 6 h, 0.4 g boric acid pre-dissolved in 20 mL water is dropped into the above mixture, thus ultimately synthesizing the SiB-TC microcapsules.

Preparation of PUA Composite Coatings: First, BN powder is treated with ultrasonic exfoliation of 12 h, with a concentration of 2 g L^{-1} in water. The BN nanosheets are collected by the continuous process of centrifugation, vacuum filtration, and freeze-drying of suspension liquid. Second, MMT nanosheets are prepared by the same method. Third, the SiB-TC microcapsules (2.0 g), BN nanosheets (0.5 g), and MMT nanosheets (2.0 g) were added to the PUA precursor (22.75 g) with the mechanical stir and sonication of 2 h, thus obtaining a uniform dispersion. Finally, the PUA curing agent (22.75 g) was added to the above solution with a rapid stir of 5 min, and poured into the mold designed to complete the curing reaction. The SiB-TC microcapsules were immersed in the ethyl alcohol solution with pH 1 to destroy the thermochromic function, further preparing the control samples with the same process.

Characterization: The fracture structure of the pure PUA and its composite coating, and TC microcapsules were observed with an XL-30 ESEM scanning electron microscope (SEM) at an acceleration voltage of 20.0 kV. Transmission electron microscopy (TEM) was used to observe BN and MMT nanosheets with a JEOL JEM-2100F transmission electron microscope at an accelerating voltage of 200 kV. Thermogravimetric analysis (TGA) was executed with a TGA Q5000 IR thermogravimetric analyzer (TA Instruments, U.S.) at a heating rate of 20 °C min^{-1}. A combustion test was performed on a cone calorimeter (Fire Testing Technology, UK) according to ISO 5660 standard procedures, with 100 × 100 × 1 mm^3 specimens. Each specimen was exposed horizontally to 35 kW m^{-2} external heat flux. All samples were tested three times. Thermogravimetric analysis-infrared spectrometry (TG-IR) was investigated with a TGA Q5000IR thermogravimetric analyzer linked to a Nicolet 6700 FTIR spectrophotometer from 20 to 700 °C at 10 °C min^{-1} (N_2 atmosphere, flow rate of 30 mL min^{-1}).

The micro-sized combustion behavior of PUA and composite coatings was performed on a microscale combustion calorimeter. Differential scanning calorimetry (DSC) was conducted using a Q25 instrument (TA, USA) at a heating rate of 5 °C min^{-1} from −20 to 50 °C under a nitrogen atmosphere. The mechanical performance of PUA composite coatings is studied by the tensile test, by a universal testing machine with a digital force gauge (DS2, ZHIQU Precision Instruments) of a 100 N load at a displacement rate of 50 mm min^{-1}. The accelerated UV-aging test is performed by a home-made light box, which is lightproof and closed. The waveband and light intensity of UV illumination are 365 nm and ≈100 W m^{-2} and irradiation time is 160 h.

Radiative Cooling Test: UV–vis–NIR spectroscopy was performed using a Perkin-Elmer LAMBDA 1050 high-performance UV–vis–NIR double-beam spectrophotometer. The emittance spectra were obtained by measuring reflectance (R) and transmittance (T), which were calculated as 1-R-T. According to Kirchhoff's law, emittance is equivalent to absorptance when an object is in thermodynamic equilibrium. Outdoor cooling performance was measured using a self-assembled radiant refrigeration performance test device in Hefei, China. A small meteorological station is established to monitor the humidity, temperature, and solar intensity. Meanwhile, a PS foam is used as a supporter, covered by the Al foil. The composite coatings covered by PE film are put on the surface of PS foam. Seven thermocouples were used to record the temperatures. There are two environment temperatures, recorded by the meteorological station and thermocouple, respectively.

EnergyPlus Simulation: The PUA/SiB-TCM/BN/MMT (Blue) composite coating covers onto the surface of the building model, excluding glass. The thickness of PUA/SiB-TCM/BN/MMT (Blue) composite coating is 3.0 mm. The IR emissivity of PUA/SiB-TCM/BN/MMT (Blue) and control are set as 98.1% and 94.9%. Meanwhile, the solar and visible absorptivity of PUA/SiB-TCM/BN/MMT (Blue) composite coating are 34.7% and 33.0%. Attributed to the destroyed thermochromic function, the solar and visible absorptivity of the control coating are 53.9% and 65.9%. Besides, the thermal conductivity, density, and specific heat capacity of PUA composite coatings are set as 0.2 W mK^{-1}, 1.0 g cm^{-3}, and 1.3 kJ $(kg \times K)^{-1}$. The critical temperatures for cooling and heating are 26 and 18 °C. A simplified residential house with dimensions of 50 m × 30 m × 9.14 m, window offset of 0.4 m, and window to wall ratio of 0.4 is tailored for *EnergyPlus* simulation. Besides, the twenty-eight climates covering the earth are detailedly introduced in Table S4 (Supporting Information). Directing at each climate, 28 representative cities and regions are employed and listed in Table S4 (Supporting Information).

Supporting Information

Supporting Information is available from the Wiley Online Library or from the author.

Acknowledgements

The authors acknowledge financial support from the Innovation and Technology Fund (ITP/023/22TP), the National Natural Science Foundation of China (22205228), PolyU Postdoc Matching Fund (1-W27C), Anhui Provincial Natural Science Foundation (2308085ME147), and Wuyi University Collaboration Fund (1-ZGD6).

Conflict of Interest

The authors declare no conflict of interest.

Data Availability Statement

The data that support the findings of this study are available from the corresponding author upon reasonable request.

Keywords

flame retardancy, high IR emissivity, passive radiative cooling, thermochromic

Received: July 19, 2024
Revised: August 26, 2024
Published online: September 23, 2024

[1] E. A. Goldstein, A. P. Raman, S. H. Fan, *Nat. Energy.* **2017**, *2*, 17143.
[2] T. Li, Y. Zhai, S. M. He, W. T. Gan, Z. Y. Wei, M. Heidarinejad, D. Dalgo, R. Y. Mi, X. P. Zhao, J. W. Song, J. Q. Dai, C. J. Chen, A. Aili, A. Vellore, A. Martini, R. G. Yang, J. Srebric, X. B. Yin, L. B. Hu, *Science.* **2019**, *364*, 760.
[3] K. Lin, S. Chen, Y. Zeng, T. C. Ho, Y. Zhu, X. Wang, F. Liu, B. Huang, C. Y. Chao, Z. Wang, C. Y. Tso, *Science.* **2023**, *382*, 691.
[4] X. Zhao, T. Li, H. Xie, H. Liu, L. Wang, Y. Qu, S. C. Li, S. Liu, A. H. Brozena, Z. Yu, J. Srebric, L. Hu, *Science.* **2023**, *382*, 684.
[5] A. Felicelli, I. Katsamba, F. Barrios, Y. Zhang, Z. Q. Guo, J. Peoples, G. Chiu, X. L. Ruan, *Cell Rep. Phys. Sci.* **2022**, *3*, 101058.
[6] a) Y. Wu, Y. Wang, S. Zhang, S. Wu, *ACS Nano.* **2021**, *15*, 15720; b) R. A. Ligon, K. J. McGraw, *Behav. Ecol.* **2018**, *29*, 1075; c) R. A. Ligon, K. J. McGraw, *Biol. letters.* **2013**, *9*, 20130892; d) A. Best, *Ann. Sci.* **1968**, *24*, 147.
[7] B. Y. Liu, J. W. Wu, C. H. Xue, Y. J. Zeng, J. Liang, S. L. Zhang, M. X. Liu, C. Q. Ma, Z. K. Wang, G. M. Tao, *Adv. Mater.* **2024**, *36*, 2400745.
[8] a) J. Chai, J. Fan, *Adv. Energy Mater.* **2023**, *13*, 2202932; b) S. Shen, L. Feng, S. Qi, J. Cao, Y. Ge, L. Wu, S. Wang, *Nano Lett.* **2020**, *20*, 2137.
[9] P. S. Aklujkar, B. J. J. o. C. T. Kandasubramanian, *Research.* **2021**, *18*, 19.
[10] Y. Y. Yin, P. C. Sun, Y. J. Zeng, M. Yang, S. W. Gao, S. Wang, Z. Y. Huang, Y. F. Zhang, Y. Wang, Z. K. Wang, *Adv. Energy Mater.* **2024**, 2402202.
[11] X. B. Shen, L. J. Cao, Y. Liu, J. Y. Dai, X. Q. Liu, J. Zhu, S. Y. Du, *Macromolecules.* **2018**, *51*, 4782.
[12] a) C. Q. Sun, *Int. Rev. Phys. Chem.* **2018**, *37*, 363; b) S. J. Grabowski, *Chem. Rev.* **2011**, *111*, 2597.
[13] L. Zhou, J. Rada, H. F. Zhang, H. M. Song, S. Mirniaharikandi, B. S. Ooi, Q. Q. Gan, *Adv. Sci.* **2021**, *8*, 2102502.
[14] S. D. Jiang, G. Tang, J. M. Chen, Z. Q. Huang, Y. Hu, *J. Hazard. Mater.* **2018**, *342*, 689.
[15] X. W. Li, Y. Z. Feng, C. Chen, Y. S. Ye, H. X. Zeng, H. Qu, J. W. Liu, X. P. Zhou, S. J. Long, X. L. Xie, *J. Mater. Chem. A.* **2018**, *6*, 20500.
[16] S. Karabulut, M. Sekerci, R. Adiguzel, Z. K. Genc, *J. Therm. Anal. Calorim.* **2023**, *148*, 10679.
[17] T. Nishi, K. Tanaka, K. Ohnuma, T. Manako, H. Ohta, S. Sukenaga, H. Shibata, T. Kakihara, *J. Nucl. Mater.* **2018**, *510*, 193.
[18] a) J. F. Watts, J. Wolstenholme, *An introduction to surface analysis by XPS and AES*, John Wiley & Sons, Hoboken, NJ, USA **2019**; b) Y. Z. Feng, C. G. He, Y. F. Wen, Y. S. Ye, X. P. Zhou, X. L. Xie, Y. W. Mai, *Compos. Part A-Appl. S.* **2017**, *103*, 74.
[19] H. N. Tran, C. C. Lin, H. P. Chao, *Sep. Purif. Technol.* **2018**, *192*, 36.
[20] X. N. Wang, W. G. Li, Z. Y. Luo, K. J. Wang, S. P. Shah, *Energ Buildings.* **2022**, *260*, 111923.
[21] a) S. H. Chen, R. Z. Xu, J. M. Liu, X. L. Zou, L. Qiu, F. Y. Kang, B. L. Liu, H. M. Cheng, *Adv. Mater.* **2019**, *31*, 1804810; b) Y. F. Pan, Y. T. Gao, J. Y. Hu, G. Y. Ye, F. Zhou, C. J. Yan, *J. Mater. Chem. B.* **2021**, *9*, 404.
[22] D. Chae, M. Kim, P. H. Jung, S. Son, J. Seo, Y. T. Liu, B. J. Lee, H. Lee, *ACS Appl. Mater. Interfaces.* **2020**, *12*, 8073.
[23] H. C. Ma, K. Q. Yao, S. L. Dou, M. Xiao, M. G. Dai, L. Wang, H. P. Zhao, J. P. Zhao, Y. Li, Y. H. Zhan, *Sol. Energ. Mat. Sol. C.* **2020**, *212*, 110584.

[24] J. L. Kou, Z. Jurado, Z. Chen, S. H. Fan, A. J. Minnich, *ACS Photonics.* **2017**, *4*, 626.
[25] Y. Zhou, H. M. Song, J. W. Liang, M. Singer, M. Zhou, E. Stegenburgs, N. Zhang, C. Xu, T. Ng, Z. F. Yu, B. Ooi, Q. Q. Gan, *Nat. Sustain.* **2019**, *2*, 718.
[26] D. Chae, S. Son, Y. Liu, H. Lim, H. Lee, *Adv. Sci.* **2020**, *7*, 202001577.
[27] Y. Yang, L. S. Long, S. Meng, N. Denisuk, G. Z. Chen, L. P. Wang, Y. G. Zhu, *Sol. Energ. Mat. Sol. C.* **2020**, *211*, 110548.
[28] H. Bao, C. Yan, B. X. Wang, X. Fang, C. Y. Zhao, X. L. Ruan, *Sol. Energ. Mat. Sol. C.* **2017**, *168*, 78.
[29] S. Meng, L. S. Long, Z. X. Wu, N. Denisuk, Y. Yang, L. P. Wang, F. Cao, Y. G. Zhu, *Sol. Energ. Mat. Sol. C.* **2020**, *208*, 110393.
[30] H. J. Kang, Y. D. Qiao, Y. Li, W. Qin, X. H. Wu, *Ind. Eng. Chem. Res.* **2020**, *59*, 15226.
[31] Y. P. Tian, H. Shao, X. J. Liu, F. Q. Chen, Y. S. Li, C. Y. Tang, Y. Zheng, *ACS Appl. Mater. Inter.* **2021**, *13*, 22521.
[32] X. Z. Ao, M. K. Hu, B. Zhao, N. Chen, G. Pei, C. W. Zou, *Sol. Energ. Mat. Sol. C.* **2019**, *191*, 290.
[33] U. Banik, A. Agrawal, H. Meddeb, O. Sergeev, N. Reininghaus, M. Götz-Köhler, K. Gehrke, J. Stührenberg, M. Vehse, M. Sznajder, C. Agert, *ACS Appl. Mater. Inter.* **2021**, *13*, 24130.
[34] S. Y. Jeong, C. Y. Tso, Y. M. Wong, C. Y. H. Chao, B. Huang, *Sol. Energ. Mat. Sol. C.* **2020**, *206*, 110296.
[35] H. W. Zhang, K. C. S. Ly, X. H. Liu, Z. H. Chen, M. Yan, Z. L. Wu, X. Wang, Y. B. Zheng, H. Zhou, T. X. Fan, *Proc. Natl. Acad. Sci. USA.* **2020**, *117*, 14657.
[36] S. Y. Heo, G. J. Lee, H. Kim, Y. J. Kim, S. Ishii, M. S. Kim, T. J. Seok, B. J. Lee, H. Lee, Y. M. Song, *Sci. Adv.* **2020**, *6*, 1906.
[37] N. N. Shi, C. C. Tsai, F. Camino, G. D. Bernard, N. F. Yu, R. Wehner, *Science.* **2015**, *349*, 298.
[38] W. C. Wu, S. H. Lin, M. M. Wei, J. H. Huang, H. Xu, Y. H. Lu, W. J. Song, *Sol. Energ. Mat. Sol. C.* **2020**, *210*, 110512.
[39] Y. Zhai, Y. G. Ma, S. N. David, D. L. Zhao, R. N. Lou, G. Tan, R. G. Yang, X. B. Yin, *Science.* **2017**, *355*, 1062.
[40] D. L. Zhao, A. Aili, Y. Zhai, J. T. Lu, D. Kidd, G. Tan, X. B. Yin, R. G. Yang, *Joule.* **2019**, *3*, 111.
[41] X. Huang, D. F. Liu, N. Li, J. F. Wang, Z. J. Zhang, M. F. Zhong, *Sol. Energy.* **2020**, *202*, 164.
[42] X. Y. Li, J. Peoples, Z. F. Huang, Z. X. Zhao, J. Qiu, X. L. Ruan, *Cell Rep. Phys. Sci.* **2020**, *1*, 100221.
[43] X. Y. Li, J. Peoples, P. Y. Yao, X. L. Ruan, *ACS Appl. Mater. Interfaces.* **2021**, *13*, 21733.
[44] Y. Liu, S. Son, D. Chae, P. H. Jung, H. Lee, *Sol. Energ. Mat. Sol. C.* **2020**, *213*, 110561.
[45] X. Xue, M. Qiu, Y. W. Li, Q. M. Zhang, S. Q. Li, Z. Yang, C. Feng, W. D. Zhang, J. G. Dai, D. Y. Lei, W. Jin, L. J. Xu, T. Zhang, J. Qin, H. Q. Wang, S. H. Fan, *Adv. Mater.* **2020**, *32*, 201906751.
[46] X. Meng, W. M. Tang, S. Y. Zhuo, J. C. Zhao, Z. X. Ren, Z. H. Sun, H. Yan, T. Y. Zhao, Z. G. Zhao, M. J. Liu, *Nano Res.* **2024**, *17*, 8472.
[47] C. Y. Cai, X. D. Wu, F. L. Cheng, C. X. Ding, Z. C. Wei, X. Wang, Y. Fu, *Adv. Funct. Mater.* **2024**, 202405903.
[48] K. J. Shayegan, S. Biswas, B. Zhao, S. H. Fan, H. A. Atwater, *Nat. Photonics.* **2023**, *17*, 891.
[49] F. X. Coudert, R. Vuilleumier, A. Boutin, *ChemPhysChem.* **2006**, *7*, 2464.
[50] E. Zojer, T. C. Taucher, O. T. Hofmann, *Adv. Mater. Interfaces.* **2019**, *6*, 201900581.
[51] F. Awaja, S. N. Zhang, M. Tripathi, A. Nikiforov, N. Pugno, *Prog. Mater. Sci.* **2016**, *83*, 536.
[52] J. J. Liu, K. Q. Zhou, P. Y. Wen, B. B. Wang, Y. Hu, Z. Gui, *Polym. Advan. Technol.* **2015**, *26*, 626.
[53] W. Cai, N. N. Hong, X. M. Feng, W. R. Zeng, Y. Q. Shi, Y. Zhang, B. B. Wang, Y. Hu, *Chem. Eng. J.* **2017**, *330*, 309.
[54] S. D. Yang, Y. S. He, J. W. Bai, J. H. Zhang, *Small.* **2023**, *19*, 202302526.
[55] S. So, J. Yun, B. Ko, D. Lee, M. Kim, J. Noh, C. Park, J. Park, J. Rho, *Adv. Sci.* **2024**, *11*, 202305067.
[56] W. T. He, P. A. Song, B. Yu, Z. P. Fang, H. Wang, *Prog. Mater. Sci.* **2020**, *114*, 100687.
[57] H. H. Liao, W. F. Duan, Y. Liu, Q. Wang, H. Wen, *J. Energy Storage.* **2021**, *35*, 102248.
[58] W. Liu, D. Zhao, Z. Y. Pan, Y. C. Shen, T. W. Wang, *Prog. Org. Coat.* **2021**, *154*, 106211.
[59] Y. F. Quan, Z. R. Zhang, R. N. Tanchak, Q. S. Wang, *J. Therm. Anal. Calorim.* **2022**, *147*, 10209.
[60] a) T. Zhang, W. Cai, F. K. Chu, F. Zhou, S. E. Liang, C. Ma, Y. Hu, *Compos. Part A-Appl. S.* **2020**, *128*, 105681; b) S. S. Han, S. S. Li, X. R. Zhang, D. Y. Liu, S. Guo, B. Z. Wang, Q. S. Meng, *Constr. Build. Mater.* **2024**, *435*, 136721; c) X. D. Qian, *Polymer Composite.* **2018**, *39*, 4637; d) R. Z. Wang, Y. Chen, Y. Y. Liu, M. L. Ma, Z. Y. Tong, X. L. Chen, Y. X. Bi, W. B. Huang, Z. J. Liao, S. L. Chen, X. Y. Zhang, Q. Q. Li, *Polym. Advan. Technol.* **2021**, *32*, 4700; e) R. Z. Wang, Y. Chen, Y. Y. Liu, M. L. Ma, Y. B. Hou, X. L. Chen, Y. Ma, W. B. Huang, *J. Colloid Interf. Sci.* **2022**, *616*, 234; f) K. P. Song, H. L. Zhang, Y. T. Pan, Z. U. Rehman, J. Y. He, D. Y. Wang, R. J. Yang, *J. Colloid Interf. Sci.* **2023**, *643*, 489; g) K. Song, X. Bi, D. Wang, Y.-T. Pan, M. Xie, J. He, D.-Y. Wang, R. Yang, *Chem. Eng. J.* **2024**, *495*, 153850; h) K. P. Song, X. Bi, C. Yu, Y. T. Pan, H. Vahabi, V. Realinho, J. Y. He, R. J. Yang, *ACS Appl. Mater. Inter.* **2024**, *16*, 7617; i) K. P. Song, X. Bi, C. Yu, Y. T. Pan, P. Xiao, J. L. Wang, J. I. Song, J. Y. He, R. J. Yang, *ACS Appl. Mater. Inter.* **2024**, *16*, 15227.
[61] H. B. Zhou, Y. X. Zhou, Y. F. Cao, Z. R. Wang, J. L. Wang, Y. Zhang, W. Pan, *Chem. Eng. J.* **2023**, *461*, 142035.
[62] L. L. An, Y. L. Yu, Q. R. Cai, S. Mateti, L. H. Li, Y. I. Chen, *Prog. Mater. Sci.* **2023**, *138*, 101154.
[63] a) D. L. Chu, H. A. Ma, J. Wang, L. X. Chen, X. P. Jia, *Ceram. Int.* **2018**, *44*, 12491; b) L. Deng, J. C. Du, *J. Am. Ceram. Soc.* **2019**, *102*, 2482.
[64] S. S. Zhou, Y. B. Yang, Z. Zhu, Z. H. Xie, X. Y. Sun, C. F. Jia, F. D. Liu, J. S. Wang, J. J. Yang, *Polymer.* **2021**, *229*, 124027.